VORTICITY DYNAMICS AND SCALAR TRANSPORT IN SEPARATED AND REATTACHED FLOW ON A BLUNT PLATE

BY

DANESH TAFTI

NATIONAL CENTER FOR SUPERCOMPUTING APPLICATIONS (NCSA)
UNIVERSITY OF ILLINOIS AT URBANA-CHAMPAIGN
URBANA, IL 61801
Tel: (217)244-7385
Fax:(217)244-2909

Published in Physics of Fluids A 5 (7), July 1993, pp.1661-1673

Abstract

Two-dimensional calculations are performed for a Reynolds number of 1000 and an effective Prandtl number of unity to study the dynamics of large scale spanwise vortices with a passive scalar field in a separation and reattaching flow over a blunt plate. A triple decomposition technique is used to isolate the quasi-periodic fluctuations related to the large scale vortices shed from the separated shear layer. Three vortex shedding modes are identified in the reattachment zone, two of which involve partial pairings. The coherent vortices shed from the reattachment zone have a dominating effect on scalar transport and act as "large scale mixers" by entraining wall scalar around their upstream periphery and free-stream scalar on their lower downstream edge. There is a definite relationship between the phase averaged perturbations (due to the presence of coherent vortices) in wall friction factor and wall scalar transport with their respective time mean maximums. On the other hand, although there does exist an explicit spatial relationship between the instantaneous stagnation point and instantaneous location of maximum wall scalar transport, there is no such relationship in the mean between the two locations, except that both are dependent on the vorticity dynamics in the reattachment region.

1. Introduction

The understanding of the fundamental mechanisms affecting heat and mass transfer in separated and reattached flows is of vital importance in a number of engineering applications. Previous studies (Ota and Kon[1]; Vogel and Eaton[2]) have shown that the heat transfer coefficient decreases from a sharp peak at the the point of separation and then increases gradually to reach a maximum near the time mean reattachment point. The exact location of the point of maximum heat transfer with respect to the time mean reattachment point (change in sign of surface shear stress) has been the subject of much debate. Early investigators assumed that the point of maximum heat transfer coincided with the reattachment point. However, later studies (Vogel and Eaton[2]; Sparrow et al.[3]), have shown that the point of maximum heat transfer lies well upstream of the time mean reattachment point.

There are a number of studies which have investigated heat transfer characteristics in different separating and reattaching geometries. Due to their relative simplicity the most common of these are the backward facing step and the blunt plate. Vogel and Eaton[2] made fluid dynamic as well as heat transfer measurements downstream of a backward facing step. They found that maximum heat transfer occurred upstream of the time mean reattachment point and coincided with the region of maximum turbulence intensity. Sparrow et al.[3] did an experimental and computational study of heat transfer over blunt cylinders and a backward facing step. They confirmed the results of Vogel and Eaton[2] that the point of maximum heat transfer was upstream of the reattachment point. They noted that the wall adjacent streamwise velocity and the transverse velocity in the wall adjacent flow had some relation to the position of maximum heat transfer. Kawamura et al.[4] tried to find a relationship between the instantaneous reattachment point and maximum heat transfer. By using the instantaneous reattachment point as a trigger to ensemble average heat transfer in its spatial vicinity, they hoped to capture the spatial dependence of maximum heat transfer in relation to the instantaneous reattachment point. However, although they found that the time averaged point of maximum heat transfer was upstream of the corresponding reattachment point, they were unable to obtain any conclusive explanation for this phenomenon.

Ota and his group have done a number of experimental studies in the general area of heat transfer in separated and reattached flows a over blunt plate and plates with different nose shapes. Ota and Kon[1] and Ota and Kon[5] measured the velocity and temperature profiles in the separated, reattached and redeveloping regions on a blunt plate and on a longitudinal blunt cylinder, respectively. Ota, Kon and Kikuchi[6] and Ota[7] measured the mean and turbulent fields for flow over a plate with different nose shapes. They found that the nose shape had a strong effect on the flow in the separated and reattachment region and even far downstream of reattachment. Nishiyama et al.[8] measured the statistical behavior of temperature fluctuations in the separated, reattached and redeveloped flow regions. They found that the location of maximum temperature fluctuations was different from that of maximum velocity fluctuations and was situated in the outer region of the separated shear layer. Ota and Kon[9] correlated the maximum heat transfer to the flow Reynolds number based on the reattachment length and found that this correlation was independent of the nose shape. An interesting observation that came out of this study was that the reattachment length increased with the nose wedge angle but the maximum heat transfer decreased. Ota and Nishiyama[10] went one step further and correlated the maximum heat transfer at reattachment in different separating flow geometries. In this correlation they used the reattachment length as the characteristic length scale and the separated shear layer velocity as the characteristic velocity.

It has been found, both experimentally (Kiya and Sasaki[11,12], Cherry et al.[13]) and via computations (Tafti and Vanka[14,15]) that the fluid dynamics of separation and reattachment is strongly influenced by the presence of large scale coherent structures in the form of spanwise vorticies. These vortices form in the separated shear layer, coalesce and grow in the reattachment region and are convected downstream (the "reattachment region or zone" will be used to denote the region between 4 and 6 plate thicknesses downstream of separation). It would not be unreasonable to assume that the presence of these large scale structures would also have a strong effect on heat-mass transfer from the reattachment surface into the free-stream. In spite of the large volume of work done in studying the heat transfer in separated flows, none of them have looked at the time dependent interaction between the temperature (scalar) field and the large scale coherent structures. Such a study would have far reaching implications not only in the geometry studied but also in other separating and reattaching geometries where such structures are known to exist.

The present study is an attempt to understand the interaction of a scalar field (temperature/species) with large scale coherent vortices in a separating and reattaching flow geometry. The geometry selected for this purpose is a blunt plate kept normal to an on coming stream of fluid and is shown in Figure 1. This geometry was chosen because of the author's previous work (Tafti and Vanka[14,15]) with it and also because it is one of the simplest separating flow geometries. The current work is a two-dimensional computational study of this geometry at a Reynolds number (based on free-stream velocity (U_∞) and plate thickness (t)) of 1000. The effective Prandtl number (Pr) for the scalar field is assumed to be unity. Although the flow characteristic of this Reynolds number is three-dimensional (Lane and Loehrke[16], Sasaki and Kiya[17]), a two-dimensional computation is able to capture the rich physics associated with the dynamics of coherent structures (Tafti and Vanka[14]). In the present work a more detailed study is performed on the different modes of vortex shedding from the reattachment zone. These modes are then isolated and averaged over a phase (Reynolds and Hussain[18]) to obtain an average field for each mode at different streamwise locations. It is found that there is strong interaction between the the large scale vortices and the corresponding scalar field.

2. Governing Flow Equations and Numerical Method

Figure 1. illustrates the coordinate system used to write the equations of motion. x (x_1) is the streamwise direction and y (x_2) is the cross-stream direction. u (u_1) is the streamwise velocity and v (u_2) is the velocity in the cross-stream direction. The time dependent two-dimensional incompressible continuity, momentum and scalar transport equations take the form:

$$\frac{\partial u_i}{\partial x_i} = 0 \tag{1}$$

$$\frac{\partial u_i}{\partial T} + \frac{\partial}{\partial x_j}(u_i\, u_j) = -\frac{\partial p}{\partial x_i} + \frac{1}{Re}\frac{\partial^2 u_i}{\partial x_j^2} \tag{2}$$

$$\frac{\partial \phi}{\partial T} + \frac{\partial}{\partial x_i}(u_i \phi) = \frac{1}{RePr}\frac{\partial^2 \phi}{\partial x_i^2} \tag{3}$$

where i, j = 1, 2. Equations (1), (2) and (3) are non-dimensionalized by the plate height (t), the free-stream approach velocity (U_∞) with $Re = U_\infty t/\nu$ and $Pr=\nu/\alpha$ (α is the scalar diffusivity). The velocity is non-dimensionalized by U_∞, length by t, time by t/U_∞ and pressure by ρU_∞^2. The non-dimensional scalar $\phi=(\theta - \theta_w)/(\theta_\infty - \theta_w)$, where θ is any scalar and the subscript w refers to the top surface of the plate and ∞ refers to the free-stream. Based on this definition, $\phi_w = 0$ and $\phi_\infty = 1$.

In the present study, higher order finite difference approximations are used for spatial discretization of the governing equations on a staggered grid. The conservative form of the convection terms are approximated by using a fifth order accurate upwind-biased approximation (similar to Rai and Moin[19], with the exception that a conservative formulation of the convection terms is used in the present formulation) and the diffusion terms are approximated by a sixth order accurate central differencing scheme. The cell face fluxes are calculated using a sixth order accurate central difference formulation. This formulation uses a thirteen point stencil for each node (parent node plus six neighbors per coordinate direction) in the calculation domain. Correspondingly, the order of approximation reduces at boundary nodes where fewer points are included in the approximation. However, care is exercised in making optimum use of boundary nodes without excessively complicating the formulation. The elliptic Poisson type equation for pressure is discretized using a second order central difference approximation for the gradient of pressure and the divergence of the velocity field. Details of the numerical scheme along with other higher differencing formulations can be found in Tafti[20]. Time integration of the momentum and continuity equations are performed using a fractional step method described in Tafti and Vanka[14]. One difference in the current formulation is that all terms in the momentum equation are treated explicitly by using the second order accurate Adams-Bashforth differencing scheme. The Poisson equation for pressure is solved by using an iterative multigrid method with the Stones Strongly Implicit formulation (Stones[21]) used to relax the solution at each grid level. The scalar equation is advanced in time by using an explicit formulation similar to the momentum equations.

3. Details of Numerical Calculations

The calculation domain and the grid used in this calculation are similar to that reported in Tafti and Vanka[14]. The calculation domain extended from -4.5 to 15.5 in the streamwise direction,and -0.5 to 4 in the cross-stream direction. The domain was resolved with 256x128 finite volume cells of non-uniform size with a grid expansion/contraction ratio within 1 ± 0.055 to resolve the shear layers which form on the front and top surface of the plate. Figure 2 shows the grid distribution in the x and y directions in terms of the the grid spacing Δx and Δy.

Inlet boundary conditions are used on the west face with U_∞=1 and ϕ_∞. On the south face a symmetry boundary condition is used. The front face of the blunt plate is maintained at ϕ_∞, with only the top surface maintained at ϕ_W. Both, at the east and north face of the computational domain an advective boundary condition of the type

$$\frac{\partial \varphi}{\partial T} + c\frac{\partial}{\partial x_i}(\varphi) = 0 \tag{4}$$

is applied, where c is a mean flow velocity normal to the boundary and subscript i =1 for the east face and i=2 for the north face. On the east face, c was set equal to 0.75, which corresponds to the bulk convection velocity of the large scale vortices convecting out of the domain (Tafti and Vanka[14], Kiya and Sasaki[11]). Since, at the north face there is no characteristic convection velocity, c was set equal to $\Delta y/\Delta T$. Figure 3 shows four time sequences of vorticity contours of a typical vortex convecting out of the calculation domain at the east face. It can be seen that the passage of the vortex is very smooth without any unphysical deformations. However, this does not give us any quantitative feel regarding spurious reflections from the boundary into the calculation domain. In view of this, a further test was performed in which a single vortex was allowed to convect out of the calculation domain (Poinsot and Lele[22]). The calculation domain and the boundary conditions used are shown in Figure 4. The initial vortex (centered at x=l and y = 0) is given by the stream function:

$$\psi = C \exp\left(-\frac{x^2 + y^2}{2R_c^2}\right) \tag{5}$$

where C is vortex strength, and R_c is the vortex radius. The calculations are done with $C/u_0 l = -0.0005$, $R_c/l = 0.15$ for a $Re = u_0 l/\nu = 1000$ and the calculation domain resolved into 80x80 finite-volume cells. The vortex is allowed to convect out of the calculation domain with a convection velocity $u_0=1.0$. Figure 5 shows three time frames at T=0, 1 and 2 of vorticity and streamwise velocity $((u-u_0)/u_0)$. As the vortex leaves the domian (T=1) there is no large scale distortion in the vorticity and velocity fields. The maximum vorticity in the calculation domain at T=2, which results from numerical reflections from the boundary is about 10^{-4} times the original vorticity. From the above two tests, it can be concluded with some degree of certainty that the advective boundary conditions used in the present study are quite adequate in providing a smooth transition for large vortical structures out of the calculation domain.

Initial conditions for the velocity field were obtained from a previous simulation (Tafti and Vanka[14]). At the start of integration the scalar field was assumed to be uniform in the free stream (ϕ_∞) with the boundary conditions applied to the blunt plate as specified above. The velocity and scalar field were then integrated for T=30 non-dimensional time units before any data was used from the simulation (all times reported are with respect to T=30 as datum).

To study the interaction of the large scale coherent structures with the scalar field, the triple decomposition scheme of Reynolds and Hussain[18] is used in which any time dependent variable S is decomposed into

$$S(p,n) = \overline{S} + \tilde{s}(p) + s'(p,n) \tag{6}$$

where S is the total fluctuating quantity, $\overline{S}$ is the time mean quantity, $\tilde{s}$ is the average at constant phase and s' is the random component. The terms in parentheses specify the functional dependence of these terms, where p indicates phase and n indicates a snapshot for each phase. The variable p has values ranging from 1 to P defining the different phases in the cycle and n ranges from 1 to N, where N is the number of snapshots for each phase p. The average at constant phase is defined by

$$\tilde{s}(p) = \frac{1}{N} \sum_{n} \{S(p,n) - \bar{S}\} \qquad (7)$$

The triple decomposition technique differs from the conventional Reynolds averaging (time averaged + random fluctuations) in that it recognizes the presence of quasi-periodic large scale coherent structures in the flow and distinguishes them from the underlying random turbulence. A number of researchers have used this technique to study the flow topology in wakes behind flat plates (Perry and Steiner[23], Kiya and Matsumara[24]) and in cylinder wakes (Cantwell and Coles[25]).

Since the aim of the current calculation is to study the interaction between the large scale structures and the scalar field, only the phase point which corresponds to the passing of such a structure at a given streamwise location is considered. It is well established by experiments (Cherry et al.[13]) and computational studies (Tafti and Vanka[14,15]) that the convection of a large scale structure has a definite velocity and pressure signature associated with it. An example of the wall pressure signal at x=6 is shown in Figure 6 for one representative cycle. As the upstream edge of the vortex approaches the location, there is a peak in the pressure signal. The subsequent valley occurs when the vortex is centered over the location, and which changes to another peak and as the vortex moves downstream. This characteristic of the wall pressure signal is used to trigger the identification and storage of a snapshot at each specified streamwise location. In the present implementation, each sub-domain (region of space surrounding triggering point) has a separate reference signal to determine the phase in that region. Since the main objective is to study the interaction between the large scale vortices and the scalar field, in the present study only one phase average corresponding to the valley in Figure 6 is obtained for each sub-domian. In essence, each large scale structured is followed, with snapshots taken at specific streamwise locations.

The wall pressure signal is monitored at five streamwise locations x=4, 5, 6, 7, and 8. A snapshot of the region surrounding the location in question is stored when the pressure signal satisfies two conditions: (a) It is less than a pre-specified threshold value; (b) The time derivative of the pressure signal changes from a negative to a positive value. The first condition makes sure that it is indeed a large scale structure which is convecting over the point and the second condition provides a criterion for aligning the structure between different snapshots. These conditional snapshots of the flow field were obtained for 288 non-dimensional time units. During this time 50, 38, 28, 28, 28 snapshots were generated at x=4, 5, 6, 7, and 8, respectively. Both, numerical data corresponding to the velocity, pressure and scalar field, and visual frames of vorticity, pressure and scalar field were stored for each snapshot. The larger number of snapshots generated at the locations x=4 and 5 are representative of vortex pairings which occur in this region and their corresponding effect on the wall pressure signal. In the post-processing stage different vorticity modes were identified by studying a combined time sequence diagram for all streamwise locations. After separating the different modes of vortex shedding from the reattachment zone, visual processing of vorticity snapshots was used to eliminate snapshots which did not fit into the ensemble. No further attempt was made to align the structures with each other before obtaining the phase average.

Simultaneously with the conditional sampling and storage of phase snapshots, the flow field was also sampled to obtain time mean flow fields and time mean turbulent statistics (in this case the fluctuation from the mean would include $\tilde{s}$ + s'). The mean flow quantities were sampled for 320 non-dimensional time units while the time mean turbulent statistics were sampled over 288 non-dimensional time units.

4. Results

Section 4.1 outlines the methodology used in identifying the different modes of vortex shedding from the reattachment zone and their subsequent phase averaging. Sections 4.2 and 4.3 discuss the physical implications of the phase averaged velocity/vorticity and scalar fields, respectively. Section 4.4 discusses the relationships between locations of maximum wall scalar transport /friction factor and the reattachment point in the context of their phase averaged and mean distributions.

4.1 Vorticity Dynamics in Separation Bubble

In order to obtain good quality phase averages from the conditional snapshots obtained at different streamwise locations, it was important to differentiate between the different modes of vortex shedding from the separation and reattachment zone. Figure 7 (a), (b) and (c) show a time sequence plot where the y axis corresponds to the 5 streamwise stations (x=4, 5, 6, 7, and 8). Each point corresponds to the presence of a large scale structure at that location based on the conditions specified in section 3. The corresponding frequency spectra for pressure fluctuations (p" = $\tilde{p}$ + p') at x=4 and x=6 are shown in Figure 8. At both locations, the dominant frequency is f=0.1 (non-dimensional), which is the characteristic vortex shedding frequency from the reattachment zone(Tafti and Vanka[14,15], Kiya and Sasaki[11] and Cherry et al.[13]). As will be seen the two peaks at f=0.05 and 0.15 on either side of the characteristic shedding frequency are a result of partial vortex pairings which occur in this region. By concentrating our attention on locations x=4 and 5, three basic modes (the term "mode" is used here to differentiate between different vortex formation processes in the reattachment zone and not between different "types" of structures) of vorticity dynamics emerge. The first and simplest pattern (Mode 1) is of type seen at $T \approx 17$, where the structure identified at $x=4$ convects to $x=5$ straight through and does not interact with any other structure which is subsequently shed from the separated shear layer. Two time frames of instantaneous spanwise vorticity corresponding to the two locations is shown in Figure 9(a). The black regions correspond to negative vorticity (vorticity shed from the separated shear layer) and the white regions to positive vorticity. The second pattern (Mode 2) is of type seen at $T \approx 5.5$ and $T \approx 24.5$. In general, this mode is characterized by an initial structure at $x=4$ which deforms and convects to $x=5$, and then pairs with another structure which is shed from the separated shear layer. Typical time frames of spanwise vorticity for the sequence beginning at $T \approx 5.5$ are shown in Figure 9(b). The third pattern (Mode 3) is physically similar to Mode 2, in that it does involve the partial pairing of two vortices but without the first vortex deforming/convecting to $x=5$. Typical occurrences of this type of interaction are at $T \approx 54$ and $T \approx 74$. Time frames of this mode of vortex shedding are shown in Figure 9(c) for the sequence beginning at $T \approx 74$. It should be noted that the dynamics which lead to the formation of Mode 2 and 3 have much longer residence times in the region between $x=4$ and 5 than Mode 1.

Some doubts were raised by one of the referees regarding the physicality of Modes 2 and 3, and their existence was attributed to numerical reflections from the open boundaries and to the effect of initial conditions. To this effect, a further test (the study on the advecting vortex in section 3 was motivated by this observation) was conducted in which the size of the computational domain was nearly doubled in each coordinate direction (x: -8.4 to 30.4t; y: -0.5 to 7.5). This was done by adding grid points to the existing grid only in the outer regions so as not to disturb the original grid distribution near the blunt plate. The total number of finite-volume cells used were 304x144. A uniform potential flow solution was used to initiate integration from time T=0. Figure 10 shows the time sequence plot similar to Figure 7. The first vortex shed from the separated shear layer is detected at x=4 at T≈20. It is also found that all three modes of vortex shedding are present in the reattachment zone. An additional test was performed with the original grid (256x128) and calculation domain, but with a potential flow solution as the initial condition (which is different from that of the main simulation). Again it was confirmed (not shown) that all three modes of vortex shedding were present. Judging from all the tests conducted, it can be concluded with confidence that the secondary modes (Modes 2 and 3) are not induced by the boundary conditions nor the initial conditions.

Having identified the three general modes of vortex interaction in the separation bubble we find that Mode 1 has 11 occurrences, with Mode 2 and Mode 3 having 7 and 10 occurrences, respectively in the current simulation. After visual inspection of vorticity snapshots for each mode, the sample size was further reduced to 10, 6 and 6 for Mode 1, 2, and 3, respectively. These steps were found to be quite adequate in having good quality representative snapshots for each mode at individual streamwise locations. To find the phase average at x=4 and x=5 the last snapshots pertaining to the shed structure were used. For example, for the shedding cycle initiated at T=24.5, the representative snapshots used for phase averaging at x=4 and x=5 are at T=32.8 and T=41.5, respectively. Figure 11 shows the 10 representative snapshots of vorticity for Mode 1 at x=6. It is seen that the coherent vortices are well aligned between snapshots. It is felt that the sample size for each mode, albeit small, is quite adequate in accomplishing the goals set for the present work, which is to study the phase averaged interaction between the large scale spanwise vortices and the scalar field. Further, it was found that the general characteristics of the phase averaged fields for the different modes were quite similar, once the resulting structure was shed from the confines of the reattachment region ($x > 4$).

4.2 Phase Averaged Velocity/Vorticity Fields

Figure 12(a) (b) and (c) show the phase averaged velocity vectors/streamlines corresponding to $\tilde{u}$ and $\tilde{v}$, and the vorticity field $\tilde{\omega}$ for the three modes of vortex shedding as represented by phase averaging the snapshots at x=4. In the discussions that follow, the term "phase averaging" will be used synonymously with "averaging at constant phase." Also, by definition (equation (7)) the phase averaged quantities are treated as perturbations on the mean flow. In Figure 12, negative streamlines represent clockwise rotation of the fluid and are representative of the vorticity shed from the separated shear layer. Positive streamlines represent the net effect of the interaction of the wall with the induced flow set up by the shed vorticity. In Figure 12(a), we see that the primary shed structure induces flow towards the wall on either side transporting free stream fluid into the wall region. Part of the free-stream fluid downstream of the primary structure is entrained into the structure and transported to the upstream side. The rest is re-directed further downstream by the wall. On the upstream side however, the entrained fluid is instrumental not only in transporting fluid from the free-stream to the wall but also from the wall into the free-stream via the large scale structure. The entrainment and re-direction of fluid by the wall results in a region of strong positive vorticity on the upstream side of the main structure. The interaction described above for Figure 12(a), is also evident for the other modes of vortex shedding in Figures 12(b) and 12(c). In both modes, the upstream region of strong positive vorticity and the entrainment of free-stream fluid on the downstream side are clearly evident.

The entrainment phenomenon on the upstream side of the main structure was observed and reported in the previous work of Tafti and Vanka[14] and was also observed in their three-dimensional simulations (Tafti and Vanka[15]). In both studies this phenomenon manifested itself in a region of strong counter-clockwise rotating fluid (positive vorticity). This region of positive vorticity was found to form in the reattachment zone and was transported with the primary vortex, about which it rotated and deformed. At that time it was thought that this phenomenon was initiated only once in the reattachment zone where two vortices were in close proximity (Tafti and Vanka[14]) like that depicted in Figure 9 at T=68.98, 12.07 and 81.92. However, it is found that this mechanism of transport induced by the primary vortex is a continuous process and is not characteristic of the reattachment zone.

Figures 13(a), (b), (c) and (d) show two-dimensional phase averaged snapshots at x=5, 6, 7, and 8 for Mode 1. It is seen that the zone of positive vorticity is deformed and stretched as the whole ensemble convects downstream. It should also be noted from the vector diagram, that the movement of fluid from the free-stream is much stronger on the upstream side of the structure than it is downstream. This result was also found by examining three-dimensional spatial correlations between pressure near the reattachment point and the three-dimensional velocity field surrounding it in the calculations of Tafti and Vanka[15]. However, the upstream flow pattern is seen to weaken as the vortex convects downstream and starts moving away from the wall as can be seen in Figure 13(d).

4.3 Phase Averaged Scalar Transport

Figures 14(a), (b), (c) and (d) show the phase averaged scalar field $\tilde{\phi}$ for x=5, 6, 7 and 8 for Mode 1. At all streamwise locations, a common pattern immerges in the distribution of $\tilde{\phi}$ and it is sketched in Figure 15. Upstream of the structure there is a region of positive $\tilde{\phi}$ (region 1), followed by a region of strong negative $\tilde{\phi}$, which extends upwards into the free-stream (region 2). This is again followed by an elongated region of positive $\tilde{\phi}$ (region 3) and a region of positive $\tilde{\phi}$ exists near the wall (region 4). This pattern exhibited by the $\tilde{\phi}$ field in the vicinity of a structure is quite universal, with changes only occurring in the relative extent and magnitude of $\tilde{\phi}$ between different streamwise locations and different modes of vortex shedding. As the vortex moves downstream, region 2 deforms and expands with the rotation of the vortex along its upstream periphery.

Figure 16(a), (b) and (c) show the phase averaged scalar field $\tilde{\phi}$ at x=4 for the three modes of vortex shedding. The general structure as depicted in Figure 15 is still applicable to all three modes, the major difference between the three being in the shape of these regions. One important difference between the $\tilde{\phi}$ distribution at x=4 and at x=5 and 6 is the relative magnitudes of $\tilde{\phi}$ in regions 1 and 3. At x=5 and 6, the magnitude of $\tilde{\phi}$ upstream of the main vortex (region 1) is larger than that in region 3. However at x=4, the positive fluctuations of $\tilde{\phi}$ in region 1 are very weak compared to those in region 3 downstream of the main vortex. This fact has important implications on the location of maximum heat transfer, which will become clearer in section 4.4.

Further insight into the transport process can be gained by studying the transport equation for $\tilde{\phi}$. This equation is similar to that derived by Reynolds and Hussain[18] for the phase averaged velocity field and is reproduced here for $\tilde{\phi}$.

$$\frac{\partial\tilde{\phi}}{\partial T} + \frac{\partial}{\partial x_i}(\bar{u}_i\tilde{\phi}) + \frac{\partial}{\partial x_i}(\tilde{u}_i\bar{\phi}) + \frac{\partial}{\partial x_i}(\tilde{u}_i\tilde{\phi}) = \frac{\partial}{\partial x_i}\left[\frac{1}{RePr}\frac{\partial\tilde{\phi}}{\partial x_i} + \overline{\tilde{u}_i\tilde{\phi}} - \langle u'\square_i\phi'\rangle + \overline{u\square_i\phi}\right] \tag{8}$$

where $\langle\ \rangle$ denotes averaging at constant phase and $\overline{}$ denotes time averaged mean. The right hand side of equation (8) can be re-written in the form

$$\frac{\partial}{\partial x_i}\left[\frac{1}{RePr}\frac{\partial\tilde{\phi}}{\partial x_i} - \langle u'\square_i\phi'\rangle + \overline{\square_i\phi''})\right]$$

where s" = $\tilde{s}$ + s' is the total fluctuation from the mean.

The scalar flux for any given phase can be represented by:

$$\tilde{J}_i = \bar{u}_i\tilde{\phi} + \tilde{u}_i\bar{\phi} + \tilde{u}_i\tilde{\phi} - \frac{1}{RePr}\frac{\partial\tilde{\phi}}{\partial x_i} + \langle u'_i \phi' \rangle\ \overline{u''_i \phi''}, \qquad \text{for } i = 1, 2 \tag{9}$$

(A) (B) (C) (D) (E) (F)

We can now proceed and quantify the contribution of each term to the scalar flux $\tilde{J}_i$. It is found for all cases that (B) dominates the transport of $\tilde{\phi}$. Physically, (B) represents the transfer of scalar flux by the action of the perturbed velocity field (due to the presence of a large scale structure) on the mean scalar field. Two representative flux vector diagrams are shown for the streamwise locations x=4 and x=6 in Figure 17(a) and (b), respectively. It is found that the flux vector diagrams look remarkably like the velocity vector diagrams for the respective streamwise location (Figures 12(a) and 13(b)). Referring to Figure 17(b) at x=6, on the downstream side of the vortex, scalar flux is transported towards the wall and into the vortex core along the lower downstream periphery. Region 3 in Figure 15 is a consequence of this process. As this fluid is transported in the vicinity of the wall, it picks up scalar from the wall and transports it into the free-stream (Region 2 in Figure 15). A similar pattern is also seen on the upstream side of the vortex, where the scalar is transported towards the wall (Region 1 in Figure 15), and then subsequently transported from the wall into the free-stream (Region 2). The zone characterized by Region 2, is the region where the corresponding fluid streams from the upstream and downstream sides of the structure meet and is instrumental in transporting scalar from the wall into the free-stream. It is not surprising that there is a strong correlation between this region and the zone of positive vorticity identified in Figure 13. In effect the vortices shed from the shear layer act as large scale "mixers" by entraining scalar from the wall region around its upstream periphery and free-stream scalar along the lower downstream periphery.

At this stage it is informative to examine the effect of the vortex on wall scalar transport which is characterized by the diffusional flux

$$\tilde{J}_w = -\frac{1}{RePr}\frac{\partial\tilde{\phi}}{\partial y}\bigg|_w = \tilde{St} = \frac{\tilde{Nu}}{Re\,Pr} \qquad (10)$$

where for heat transfer $\tilde{St}$ is the Stanton number and $\tilde{Nu}$ is the Nusselt number at constant phase, respectively. This distribution is shown in Figure 18 for x=6, which is an accurate representation of all streamwise locations (x>4) and even across different modes of vortex shedding. In interpreting this distribution, it should be kept in mind that in the mean the net scalar flux at the wall ($\bar{St}$) is negative (ϕ_w=0,ϕ_∞=1) (scalar transport is in negative direction). Since $\tilde{St}$ is a perturbation on the mean ($\bar{St}$), then a negative $\tilde{St}$ indicates an augmentation of scalar transfer at the wall while on the other hand a positive $\tilde{St}$ indicates an attenuating effect. On the far upstream side of the vortex (region 1 in Figure 15), diffusive scalar transport at the wall is augmented by the transport of free-stream fluid into this region. Region 2, however, acts to reduce scalar transport at the wall due to a reduction in the effective gradient. Region 3 and 4 act analogous to 1 and 2, respectively, albeit on a smaller scale.

4.4 Relationship between Maximum Wall Scalar Transport, Maximum Friction Factor and Mean Reattachment Point

As stated in the Introduction, a number of studies have attempted to explain the relationship between the mean reattachment point and the point of maximum heat transfer. The majority of studies on separating and reattaching flows (Vogel and Eaton[2]; Sparrow et al.[3]; Ota and Kon[1]) have found that the point of maximum heat transfer lies upstream of the mean reattachment point. This result is confirmed in the present two-dimensional study.

However in the present work, the basis of attempting to compare the mean reattachment point and the point of maximum heat/scalar transfer transport is questioned. In the author's opinion it would be more appropriate to compare the point of maximum heat transfer with the corresponding maximum in friction factor (rather than zero friction factor). In the following paragraph a rationale for the relationship between the two locations is provided by using the phase averaged data (in the context of the discussion that follows it would be advantageous to treat "phase averaged" data as "averaged instantaneous" data) in the reattachment region between x=4 and 6.

Figure 19(a) shows the streamwise distribution of the mean friction factor defined by:

$$\frac{\overline{C}_f}{2} = \frac{1}{Re}\frac{\partial \overline{U}}{\partial y}\bigg|_w \tag{11}$$

and its phase averaged counterpart $(\overline{C}_f+\tilde{C}_f)/2$ at different streamwise locations. Similarly, Figure 19(b) shows the equivalent scalar(heat) transfer analog ($\overline{St}$, $\overline{St}+\tilde{St}$). Maximum $\overline{C}_f$ occurs at x=4.84 with a zero value (mean reattachment length) at x=6.1. Correspondingly, the maximum wall scalar transport $\overline{St}$ occurs at x= 5.35. Using equation (10), the maximum $\overline{Nu}$ is 13.74 which agrees quite well with the correlation of Ota and Kon[1] ($Nu = 0.0782\,Re^{.709}$ for 2720<Re<17900 (length scale is based on half thickness of the plate)) which gives a value of 12.82 for the Reynolds number of 1000 (based on plate thickness). For both the friction factor and the scalar transport there is a strong correlation between the maximum fluctuations in $(\overline{C}_f+\tilde{C}_f)/2$ and $\overline{St}+\tilde{St}$ due to the presence of a vortex in the region between x=4 and 6 and the corresponding maximums in $\overline{C}_f$ and $\overline{St}$.

The difference in locations of the maximums in $\overline{C}_f$ and $\overline{St}$ can be related to their phase averaged values and hence to the characteristics of the coherent structures themselves. For Mode 1 of vortex shedding in the reattachment zone at x=4 and 5, the negative peaks in $(\overline{C}_f+\tilde{C}_f)/2$ and $\overline{St}+\tilde{St}$ are at about the same location. However, if we look at similar plots for Modes 2 and 3 we see differences between the two negative peaks which is consistent with the behavior of their respective time mean values. These are shown in Figure 20(a) for Mode 2 and 20(b) for Mode 3. Because of the elongated nature of these structures in the region between x=4 and 5 (see Figure 9), there is considerable difference between negative peaks in $(\bar{C}_f+\tilde{C}_f)/2$ and $\bar{St}+\tilde{St}$, the peak in $\bar{St}+\tilde{St}$ occurring downstream of the corresponding peak in $(\bar{C}_f+\tilde{C}_f)/2$. This effect when looked at in the time mean framework is considerably strengthened by the long residence times of these modes in the region between x=4 and 6.

Further insight into this can be gained by looking at the scalar transport equivalent of the reverse flow fraction (defined as the percentage of time the instantaneous streamwise velocity is negative). The equivalent fraction (which will be called "scalar fraction" (ϕ_f) for want of a better name) for the scalar equation is defined as the percentage of time the instantaneous scalar ϕ is less than $0.5(\phi_\infty - \phi_w)$. Physically, at a given spatial location a high percentage value of ϕ_f indicates a predominance of fluid at ϕ_w while a value less than fifty percent indicates the opposite. Figure 21 shows contours of ϕ_f in the region between separation and x=7. In the region near x=3.5, the contours of ϕ_f extend far into the free-stream indicating the predominant transport of wall scalar into the free-stream. However, in the region of maximum heat transfer (x=5.35), the contours are crowded in the wall region indicating pre-dominant transport of scalar from the free-stream. This is a result of the long residence time of vorticity modes 2 and 3 in this region and the effective transport of free-stream fluid on their downstream side.

Although, we can extrapolate from the phase averaged profiles to the mean profiles to establish a relationship between the locations of maximum friction factor and heat transfer, the same cannot be done for the phase averaged stagnation streamline (zero $(\bar{C}_f+\tilde{C}_f)/2$) and the time mean reattachment point. Firstly, the instantaneous stagnation point or reattachment point is not fixed in a spatial context and convects along with the large scale vortex. Secondly, at the location of the mean reattachment point, the reverse flow fraction (defined above) has a value of 0.5 (Tafti and Vanka[14,15]). This implies that the instantaneous streamwise velocity at this location is negative/positive fifty percent of the time and the positive/negative fluctuations are of equal magnitude in the mean. Based on these observations, the mean reattachment point does not have any explicit relationship to the phase averaged or instantaneous stagnation point, but rather to the equality of positive and negative fluctuations at that location as the large scale structures convect through. In view of this, there is no basis in attempting to compare the equality/inequality of the location of mean reattachment to the mean location of maximum heat transfer.

5. Conclusions

The current work is an attempt to study the dynamics of large scale spanwise vortices with a scalar field in a separation and reattaching flow over a blunt plate. The two-dimensional calculations are performed for a Reynolds number of 1000 and an effective Prandtl number of unity. A triple decomposition technique is used to isolate the quasi-periodic fluctuations related to the large scale vortices shed from the separated shear layer. To obtain the averages at constant phase, three vortex shedding modes are identified in the reattachment zone. Through the study of phase averaged velocity and scalar fields it is found that the presence of a vortex at a given streamwise location has a profound influence on the transport and mixing of scalar. In the vicinity of a vortex, the phase averaged scalar field exhibits a universal pattern once the vortex is shed from the reattachment zone. The vortex acts as a "large scale mixer" by entraining wall scalar around its upstream periphery and free-stream scalar on its lower downstream edge.

There is a definite relationship between the phase averaged perturbations (due to the presence of coherent vorticity) in wall friction factor and scalar transport with their respective time mean maximums. The maximum in these perturbations occurs in the reattachment region about 4 to 6 plate thicknesses downstream from separation. In the current study, the basis of attempting to compare the locations of maximum heat transfer and the time mean reattachment point is questioned. In the authors opinion, there is a firmer basis for comparing the location of maximum scalar transport with the corresponding location of maximum friction factor. The relationship between these two locations is explained in terms of their phase averaged profiles. On the other hand, although there does exist an explicit relationship between the instantaneous stagnation point and instantaneous location of maximum wall scalar transport, there is no such relationship in the mean between the two locations, except that both are dependent on the vorticity dynamics in the reattachment region.

In closing, it should be noted that the current study neglects the three-dimensional vorticity dynamics in the reattachment zone. However, the author feels that the established basis of comparing the maximum wall scalar transfer and friction factor is still legitimate, if in spite of the three-dimensionality, structures of coherent spanwise vorticity are the dominant mode of transport. Admittedly, in the laboratory flow (or a three-dimensional simulation), the degree of coherence will be markedly less with incoherent turbulence playing a larger role in the transport process. A future three-dimensional study plans to address these issues.

Acknowledgements

The author would like to acknowledge Cray-2 time provided by the National Center for Supercomputing Applications (NCSA) at the University of Illinois, Urbana/Champaign.

The author would also like to acknowledge the support and motivation provided by Dr. Pratap Vanka in the initiation of this work.

References

[1]Ota, T. and Kon, N., "Heat Transfer in the Separated and Reattached Flow on a Blunt Plate," J. Heat Transfer 96, 459 (1974).

[2]Vogel, J. C. and Eaton, J. K., "Combined Heat Transfer and Fluid Dynamic Measurements Downstream of a Backward-Facing Step," J. Heat Transfer 107, 922 (1985).

[3]Sparrow, E. M., Kang, S. S. and Chuck, W., "Relation between the points of flow reattachment and maximum heat transfer for regions of flow separation," Int. J. Heat Transfer 30(7), 1237 (1987).

[4]Kawamura, T., Tanaka, S., Mabuchi, I. and Kumada, M., "Temporal and Spatial Characteristics of Heat Transfer at the Reattachment Region of a Backward-Facing Step," Experimental Heat Transfer 1, 299 (1987-1988).

[5]Ota, T. and Kon, N., "Heat Transfer in an Axisymmetric Separated and Reattached Flow Over a Longitudinal Blunt Cylinder," J. Heat Transfer 99, 155 (1977).

[6]Ota, T. and Kon, N., "Temperature and Velocity Fields in the Separated and Reattached Flow over Blunt Flat Plate," Bull. JSME 23(177), 402 (1980).

[7]Ota, T., " Nose Shape Effects on Turbulence in the Separated and Reattached Flow over Blunt Plate," Z. Flugwiss. Weltraumforsch. 7(5), 316 (1983).

[8]Nishiyama, H., Ota, T. and Sato, K., "Temperature fluctuations in a separated and reattached turbulent flow over a blunt flat plate," Warme- und Stoffubertragung 23, 275 (1988).

[9]Ota, T. and Kon, N., "Heat Transfer in the Separated and Reattached Flow over Blunt Flat Plate - Effects of Nose Shape," Int. J. Heat mass Transfer 22, 197 (1979).

[10]Ota, T. and Nishiyama, H., "A correlation of maximum turbulent heat transfer coefficient in reattachment flow region," Int. J. heat Mass Transfer 30(6), 1193 (1987).

[11]Kiya, M. and Sasaki, K., "Structure of a turbulent separation bubble,"J. Fluid Mech. 137, 83 (1983).

[12]Kiya, M. and Sasaki, K., "Structure of large-scale vortices and unsteady reverse flow in the reattaching zone of a turbulent separation bubble," J. Fluid Mech. 154, 463 (1985).

[13]Cherry, N.J., Hillier, R., and Latour, M.P., Unsteady measurements in a separated and reattaching flow," J. Fluid Mech. 144, 13 (1984).

[14]Tafti, D. K. and Vanka, S. P., "A numerical study of flow separation and reattachment on a blunt plate," Phys. Fluid A 3(7), 1749 (1991).

[15]Tafti, D. K. and Vanka, S. P. "A three-dimensional numerical study of flow separation and reattachment on a blunt plate," Phys. Fluid A 3(12), 2887 (1991).

[16]Lane, J. C. and Loehrke, R. I., "Leading Edge Separation From a Blunt Plate at Low Reynolds Number," J. Fluids Engg. 102, 494 (1980).

[17]Sasaki, K. and Kiya, M., "Three-Dimensional Structure in a Leading-Edge Separation Bubble at Moderate Reynolds Numbers," J. Fluids Engg. 113, 405 (1991).

[18]Reynolds, W. C. and Hussain, A. K. M. F., "The mechanics of an organized wave in turbulent shear flow. Part 3. Theoretical models and comparisons with experiments," J. Fluid Mech. 54(2), 263 (1972).

[19]Rai, M. and Moin, P., "Direct Simulations of Turbulent Flow using Finite-Difference Schemes," AIAA-89-0369 (1989).

[20]Tafti, D. K., "A Study of Higher Order Spatial Finite-Difference Formulations for the Incompressible Navier-Stokes," submitted for presentation at the AIAA 11th Computational Fluid Dynamics Conference, July 6-9 1993, Orlando, Florida.

[21]Stone, H. L., "Iterative Solution of Implicit Approximations of Multidimensional Partial Differential Equations," SIAM J. Numer. Anal. 5(3), 530 (1968).

[22]Poinsot, T. J. and Lele, S. K., "Boundary Conditions for Discrete Simulations of Compressible Viscous Flows," J. Comp. Physics 101, 104 (1992).

[23]Perry, A. E. and Steiner, T. R., "Large-scale structures in turbulent wakes behind bluff bodies. Part 1. Vortex formation processes", J. Fluid Mech. 174, 233 (1987).

[24]Kiya, M. and Matsumura, M., "Incoherent turbulence in the near wake of a normal plate," J. Fluid Mech. 190, 343 (1988).

[25]Cantwell, B. and Coles, D., "An experimental study of entrainment and transport in the turbulent near wake of a circular cylinder," J. Fluid Mech. 136, 321 (1983).

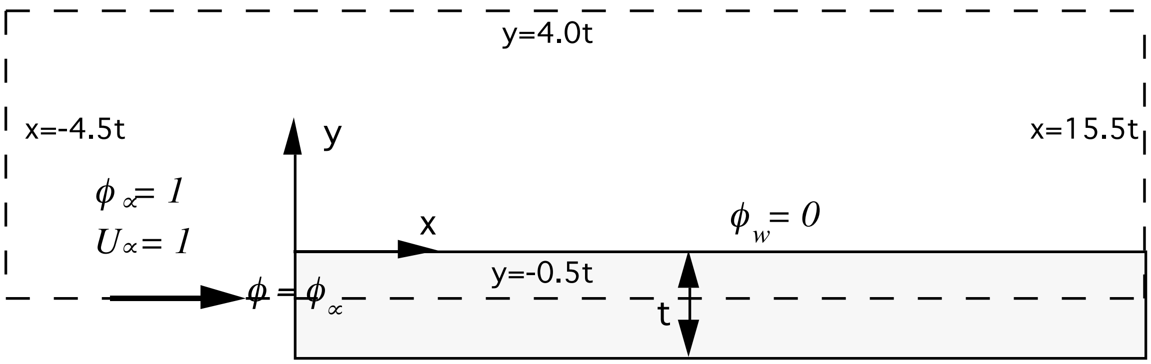

Figure 1: Flow geometry and coordinate system.

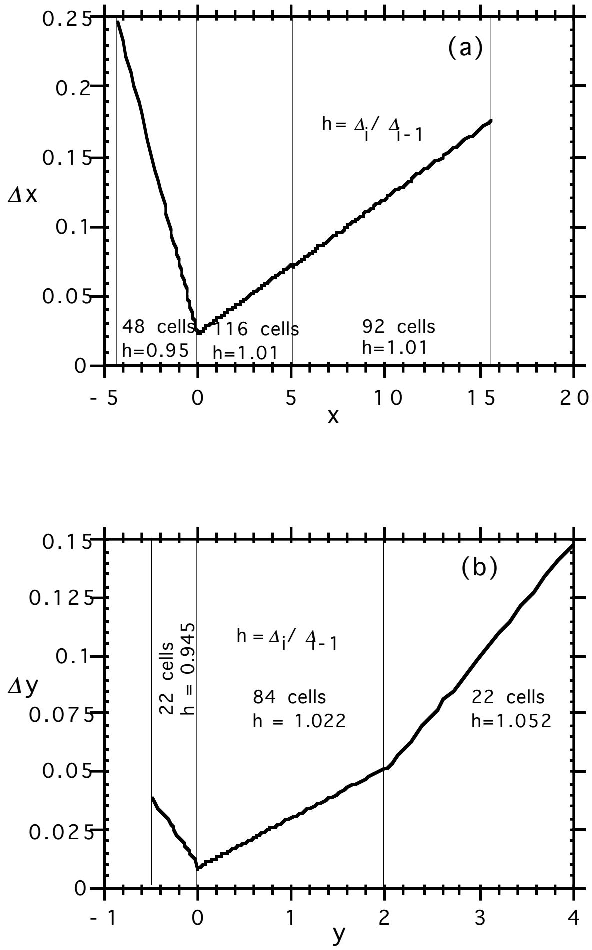

Figure 2: Computational grid distribution. (a) Streamwise direction; (b) Cross-stream direction. *h* is the grid expansion/contraction ratio.

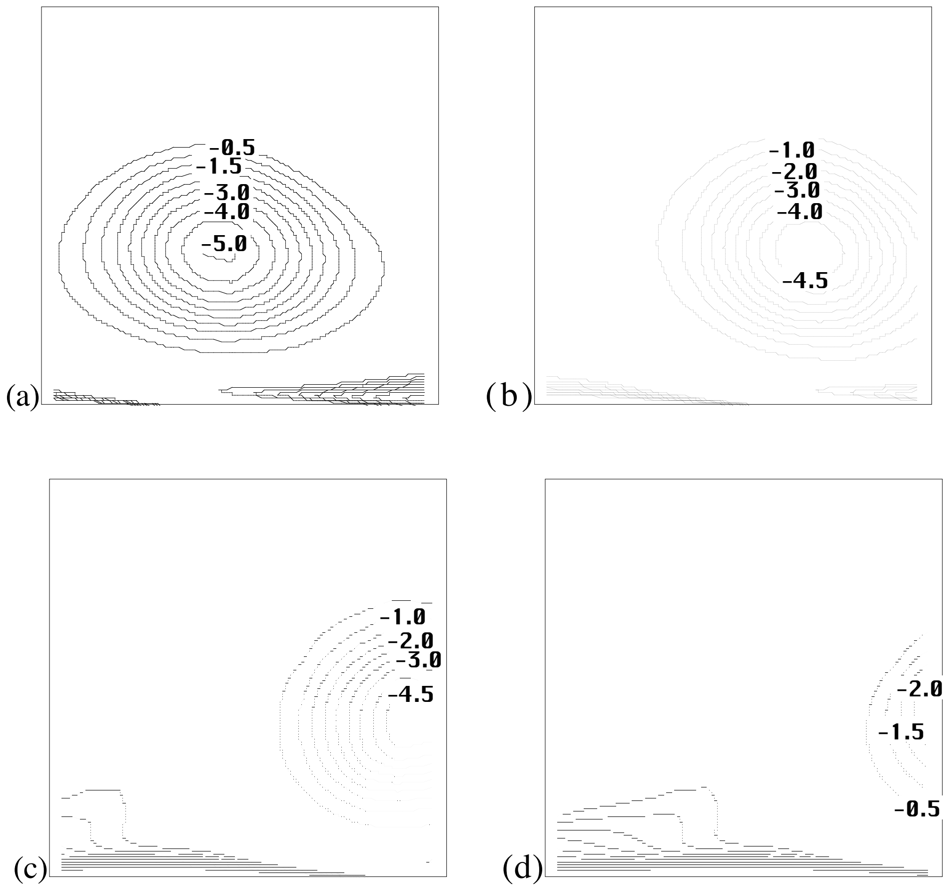

Figure 3: Four typical time frames of vortex convecting out at east face of computational domain.

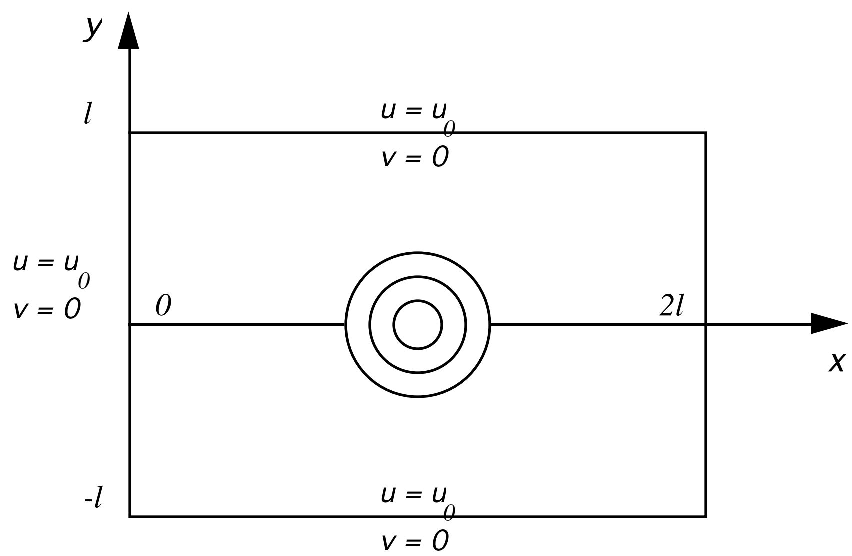

Figure 4: Geometry and boundary conditions for advecting vortex test case.

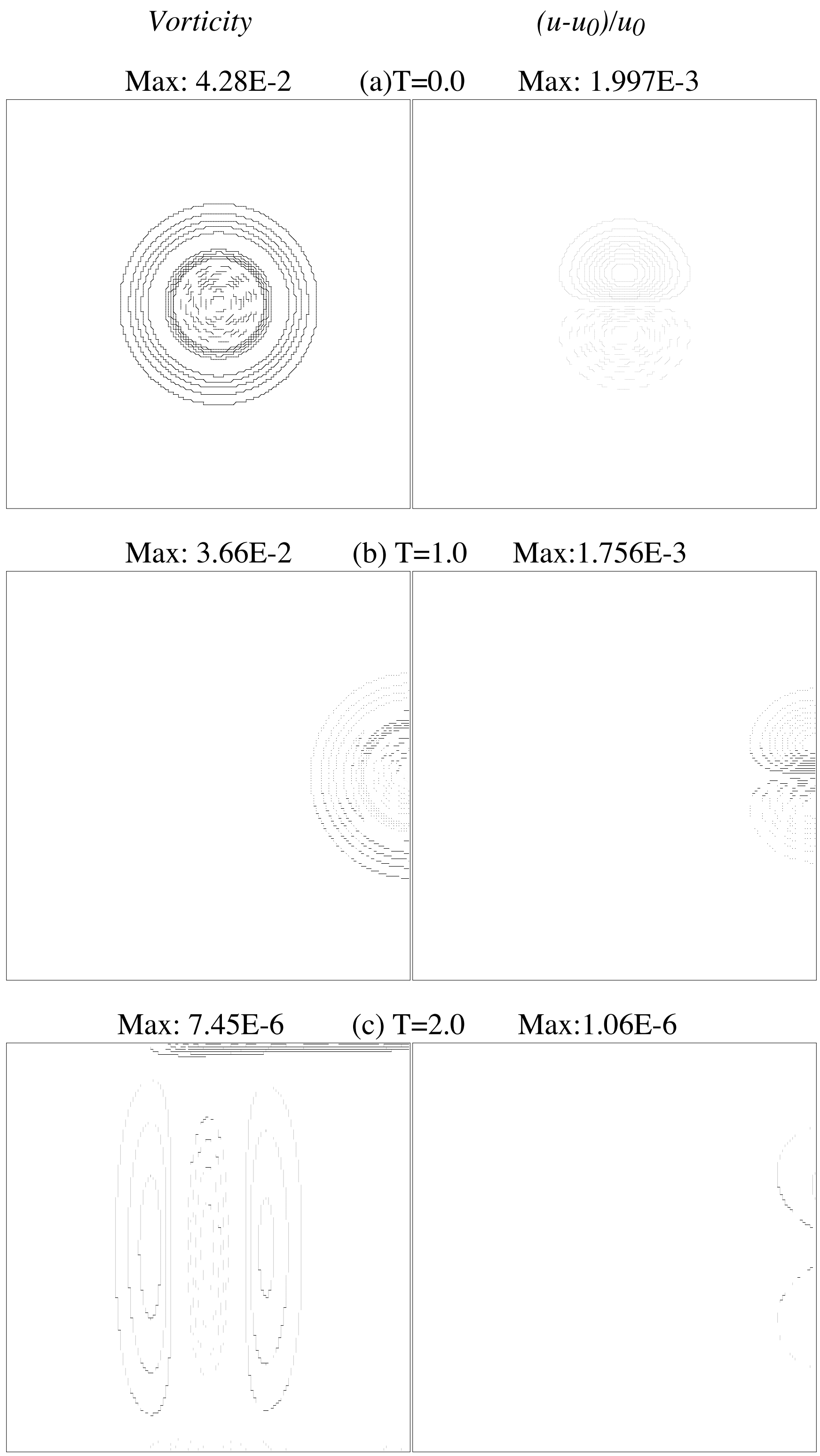

Figure 5: Contours of vorticity and streamwise velocity perturbations for advecting vortex at (a) T=0.0; (b)T=1.0; (c)T=2.0. T is non-dimensional time based on u_0 and l.

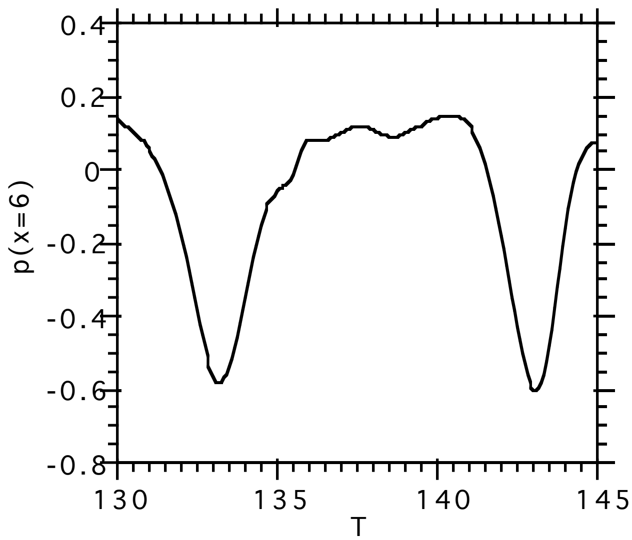

Figure 6: Wall pressure trace at x=6 for one representative cycle. The valleys correspond to the presence of a large scale vortex at this location.

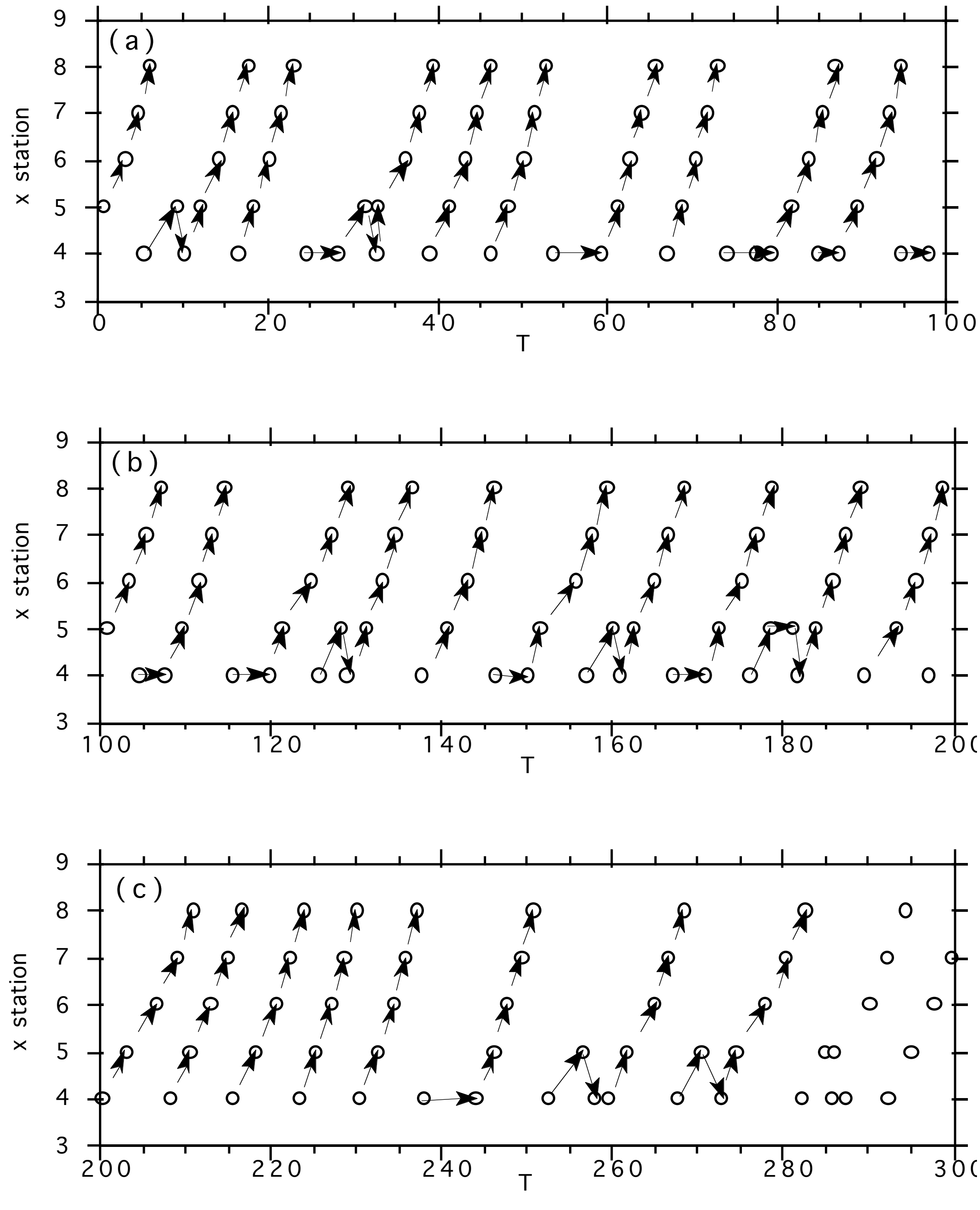

Figure 7: Combined time sequence diagram for all streamwsie locations. The circles indicate the presence of a vortex at that location. The arrows show the sequence of events for each shedding from the reattachment zone.

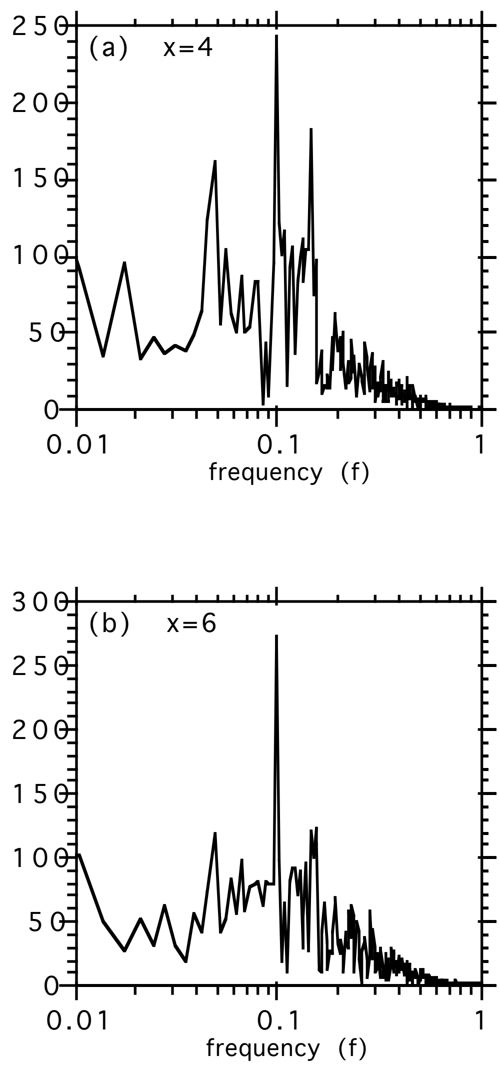

Figure 8: Frequency spectra of wall pressure fluctuations ($p'' = \tilde{p} + p'$) at (a) x=4 , and (b) x=6.

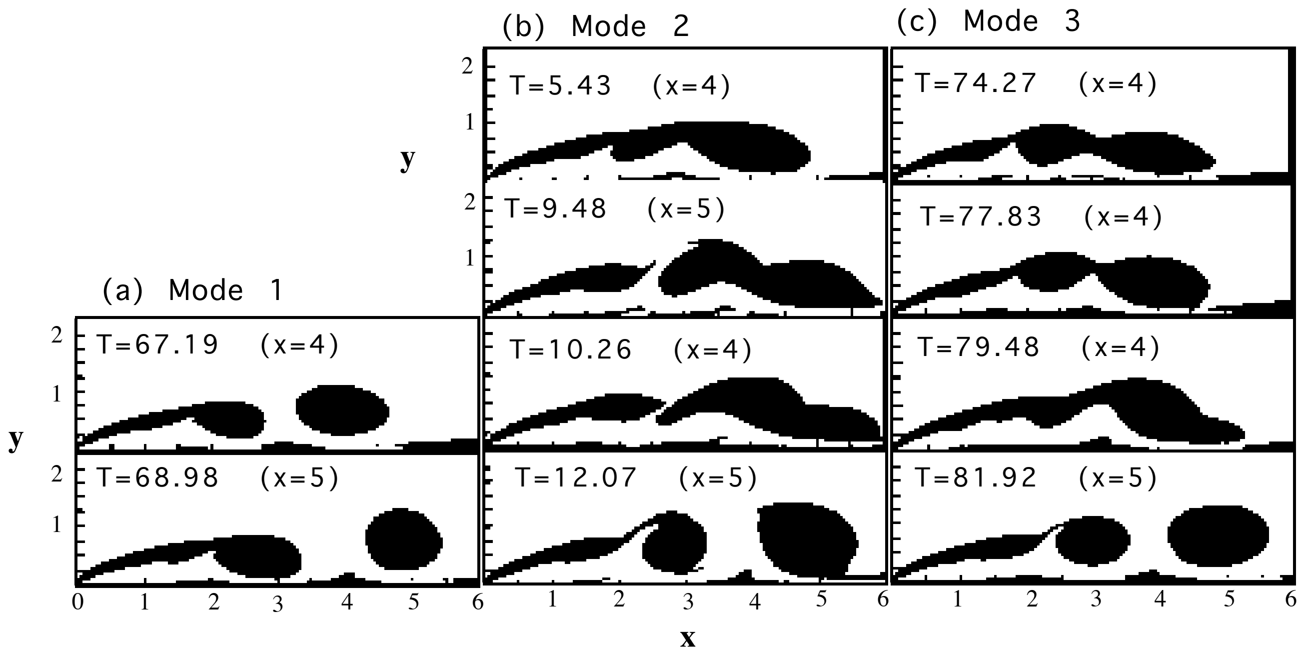

Figure 9: Representative time frames of total spanwise vorticity for the three modes of vortex shedding encountered in the reattachment region. The x locations specify the x station in Figure 7.

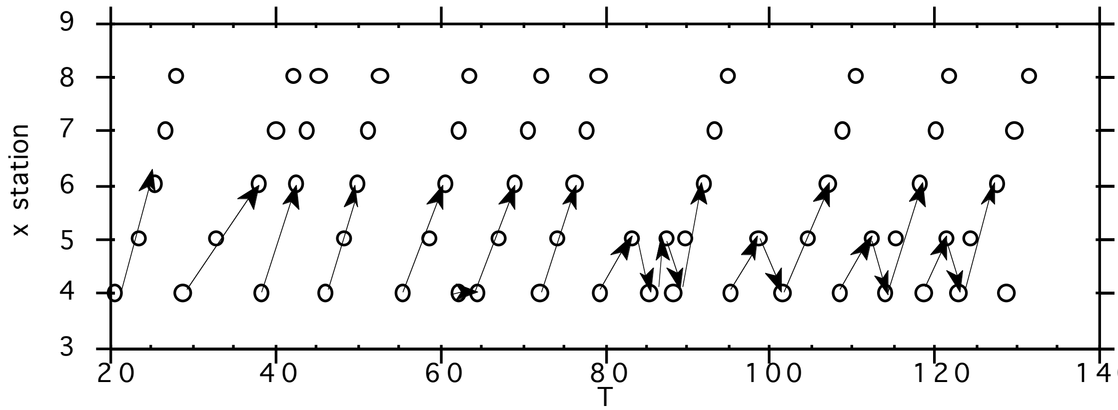

Figure 10: Time sequence diagram with larger computational domain (304x144 cells). x: -8.4 to 30.4 and y: -0.5 to 7.5.

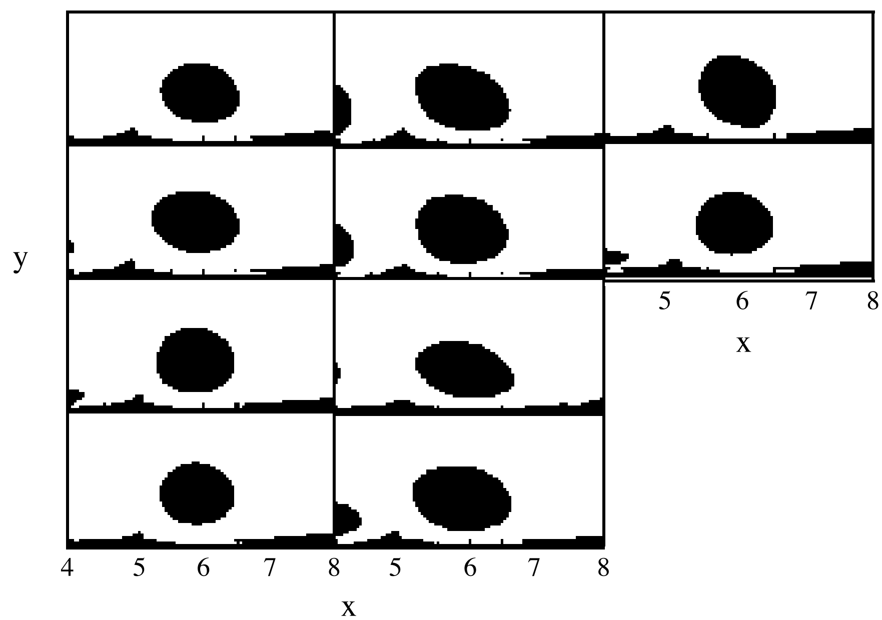

Figure 11: Representative snapshots of total spanwise vorticity for Mode 1 at x=6. These snapshots are used to obtain the average at constant phase.

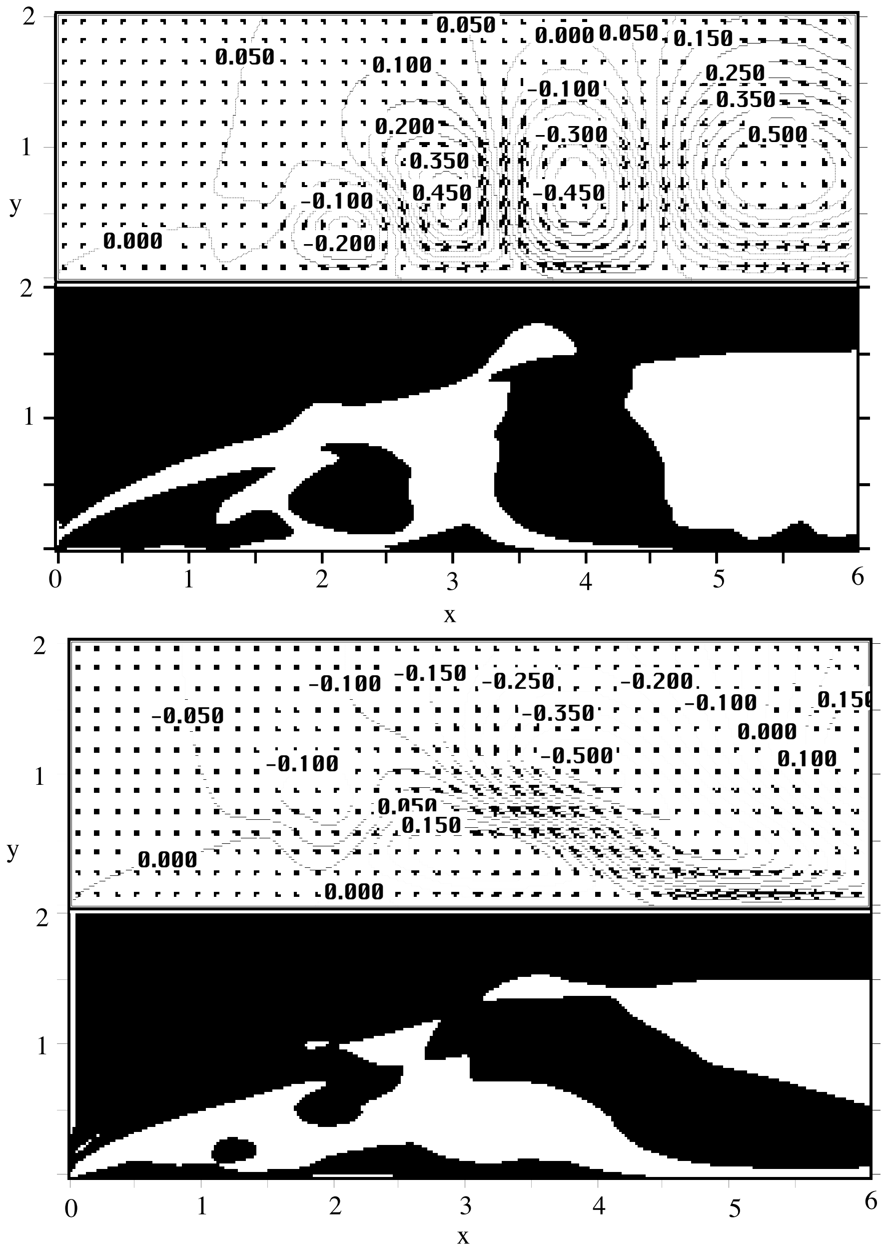

0.050
0.000
0.150
0.100
0.250
-0.100
0.350
0.200
-0.300
0.500
0.350
0.450
-0.450
-0.200
y
x
-0.150
-0.250
-0.350
-0.500
0.150
0.050

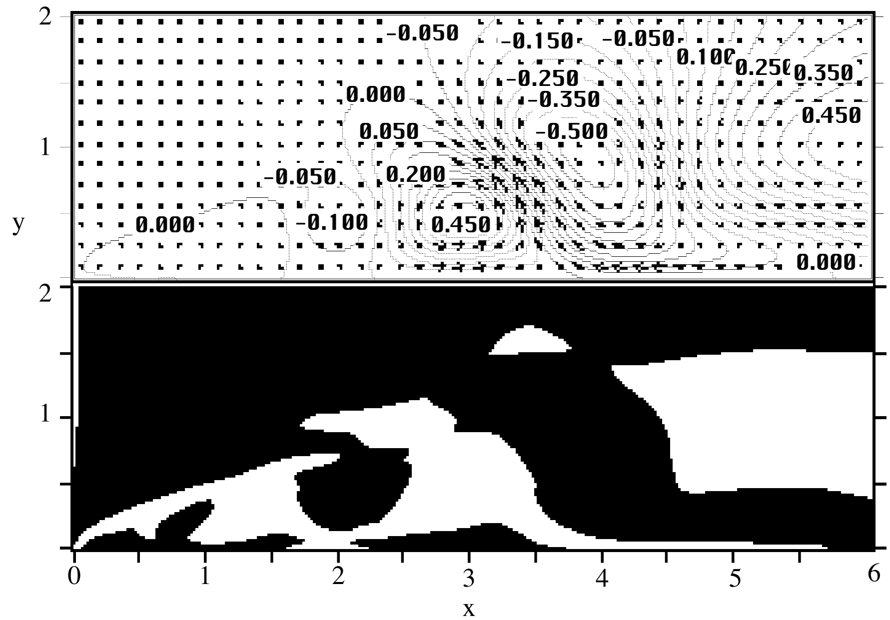

Figure 12: Phase averaged velocity vectors/streamlines ($\widetilde{u}$,$\widetilde{v}$) and vorticity field $\widetilde{\omega}$ for the three modes of vortex shedding at x=4. (a) Mode 1; (b) Mode 2; (c) Mode 3. The dashed lines correspond to negative vorticity (primary vortex shed from the shear layer) and the solid lines to positive vorticity.

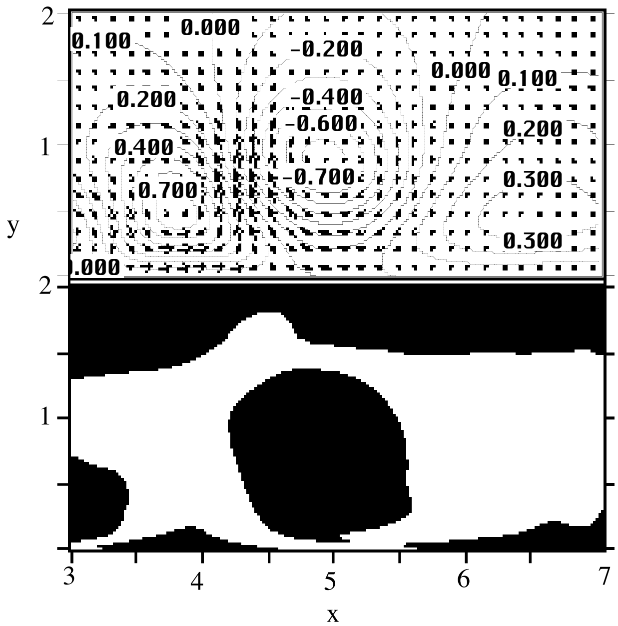
0.000
0.100
-0.200
0.000
0.100
0.200
-0.400
-0.600
0.200
0.400
-0.700
0.300
0.700
0.300
y
x

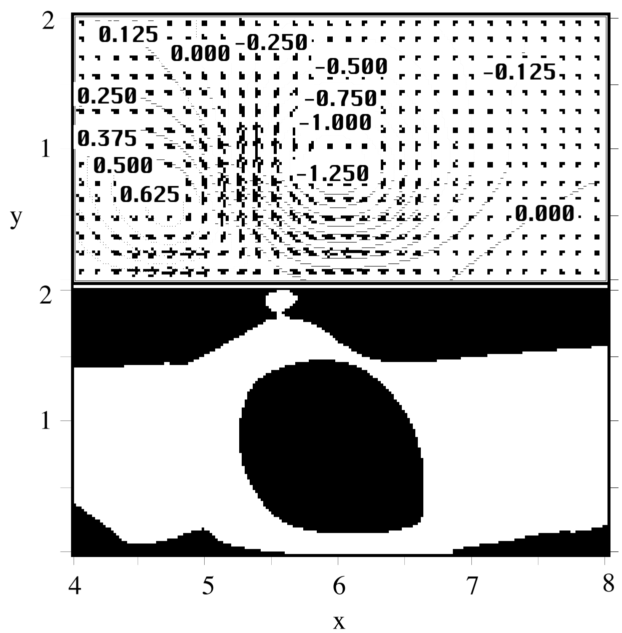
0.125
0.000
-0.250
-0.500
-0.125
0.250
-0.750
-1.000
0.375
0.500
-1.250
0.625
0.000
y
x

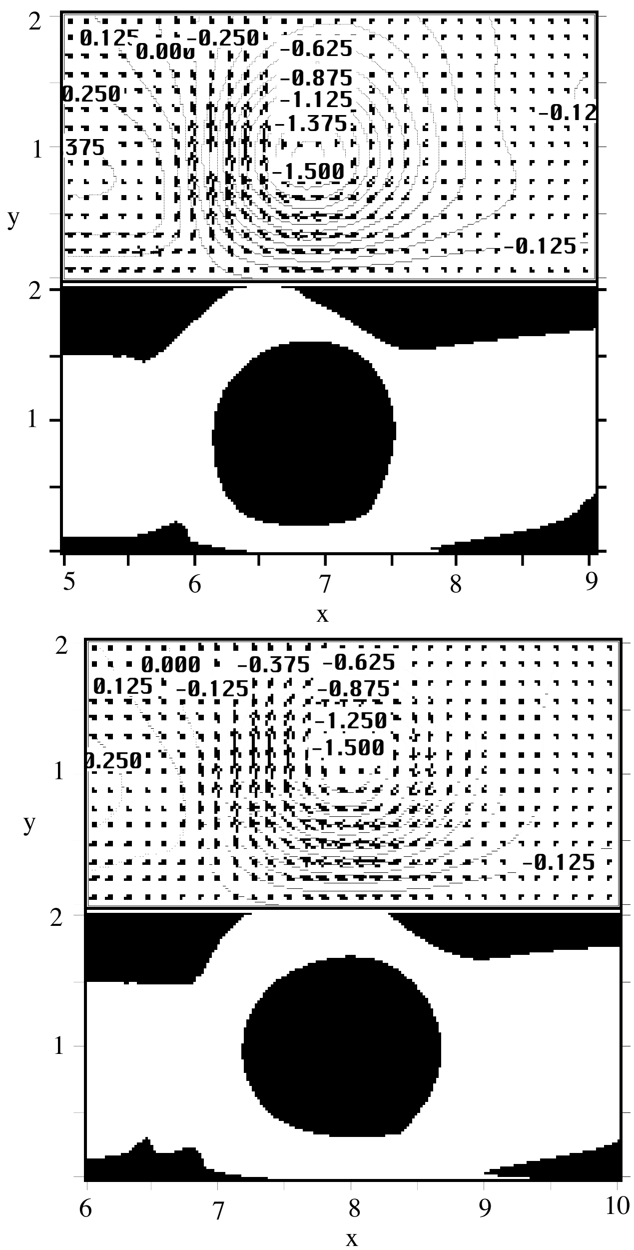

Figure 13: Phase averaged velocity vectors $(\tilde{u},\tilde{v})$ and vorticity field $\tilde{\omega}$ for Mode 1 at (a) x=5; (b)x=6; (c)x=7; (d)x=8.

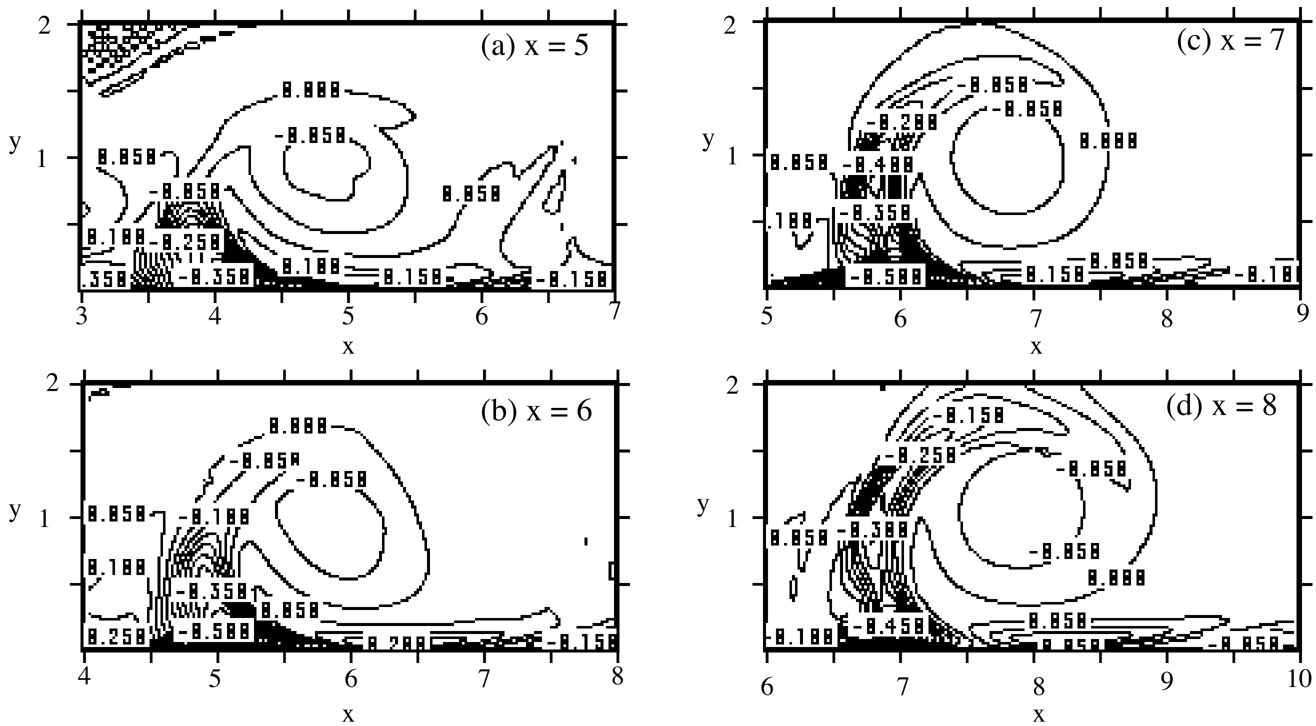

Figure 14: Contours of phase averaged scalar field ($\widetilde{\phi}$) for Mode 1 vortex shedding at (a)x=5; (b)x=6; (c)x=7; (d)x=8.

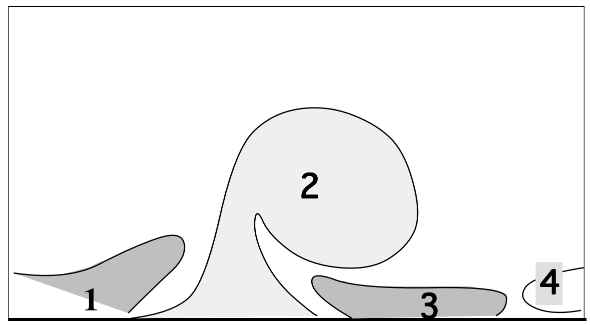

Figure 15: Schematic of general structure of phase averaged scalar field ($\widetilde{\phi}$) in the vicinity of a large scale spanwise vortex.

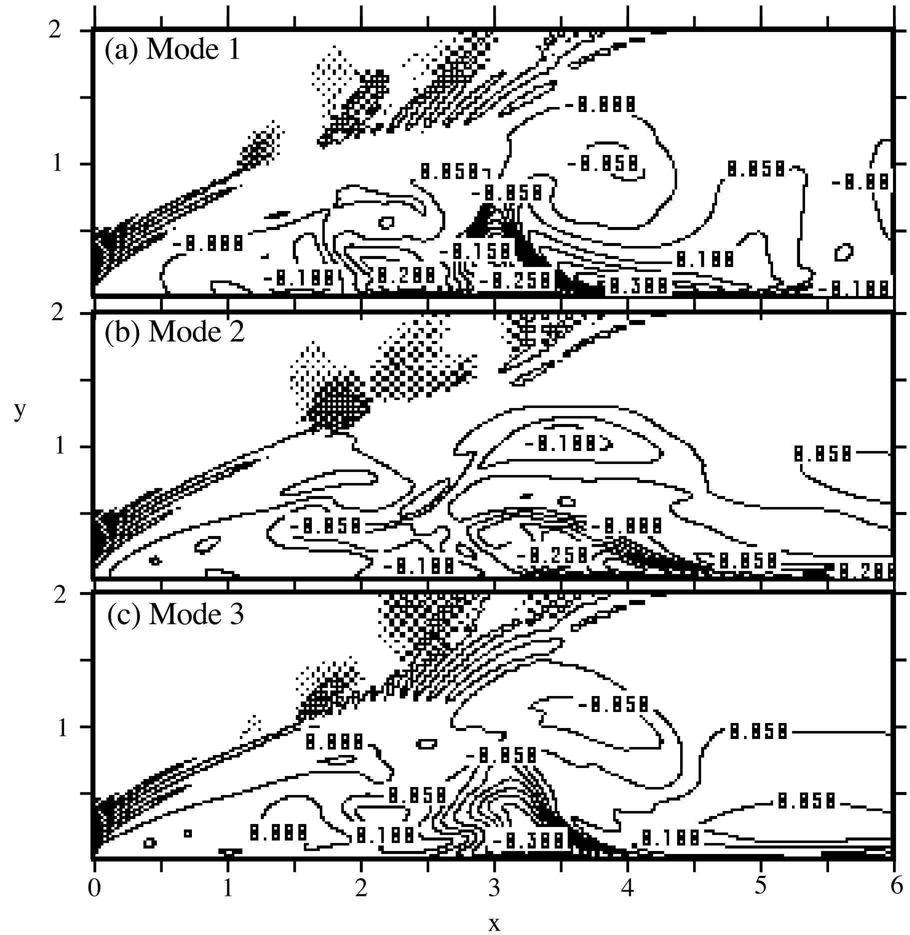

Figure 16: Contours of phase averaged scalar field ($\tilde{\phi}$) at x=4 for (a)Mode 1; (b)Mode 2; (c)Mode 3.

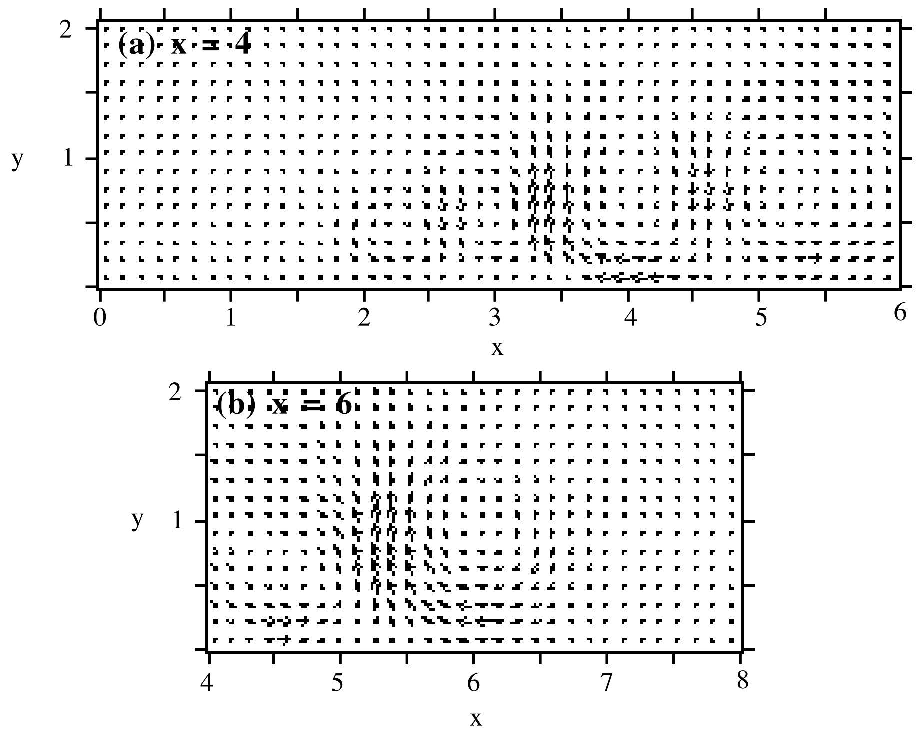

Figure 17: Flux vector diagram ($\tilde{J}$) for the transport of phase averaged scalar flux at (a)x=4; (b)x=6 for Mode 1 vortex shedding.

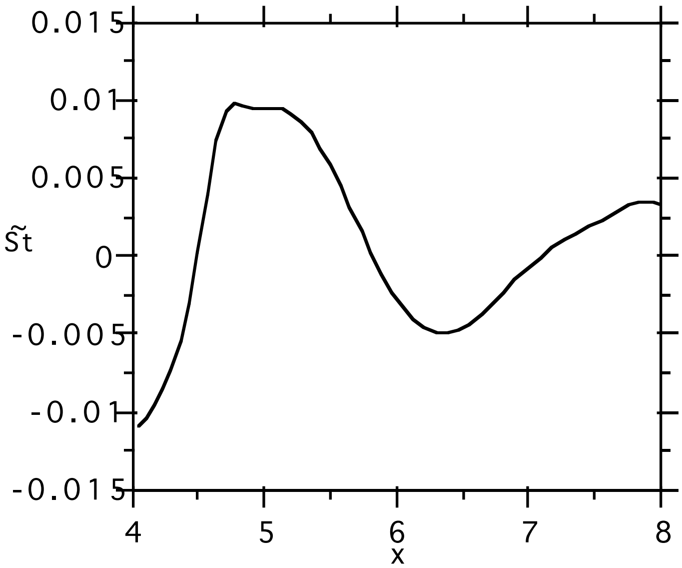

Figure 18: Streamwise variation of phase averaged Stanton number ($\tilde{St}$) in the presence of a vortex at x=6 for Mode 1 vortex shedding.

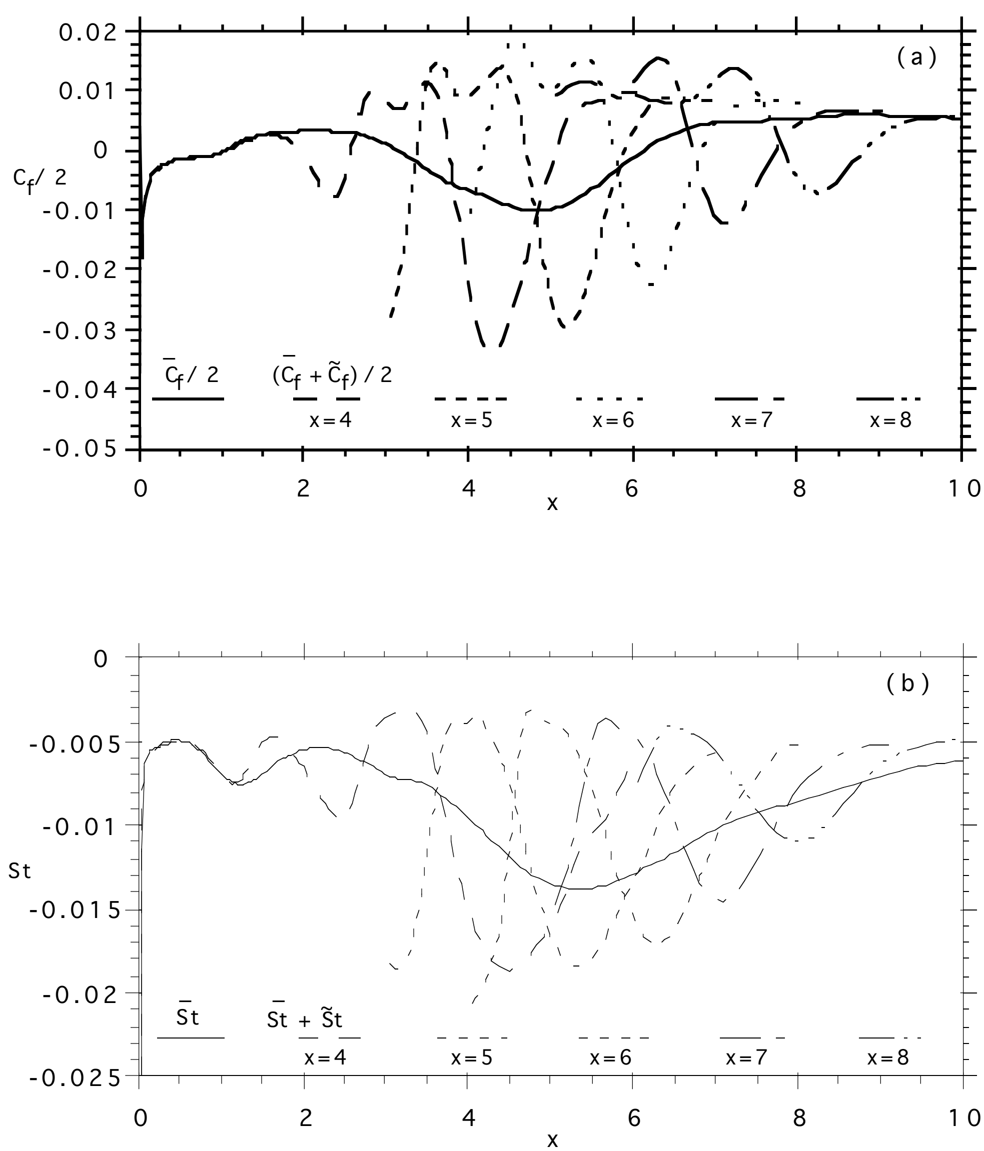

Figure 19: Variation of (a) time mean friction factor ($\bar{C}_f/2$) and phase averaged friction factor $(\bar{C}_f+\tilde{C}_f)/2$ caused by the presence of large scale vorticity (Mode 1) at different streamwsie locations; (b) Scalar transport equivalent for Mode 1.

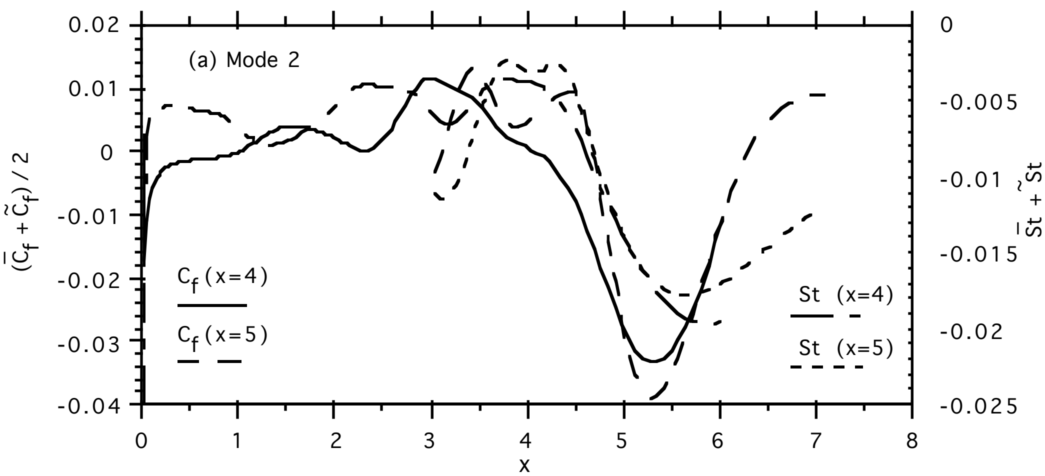

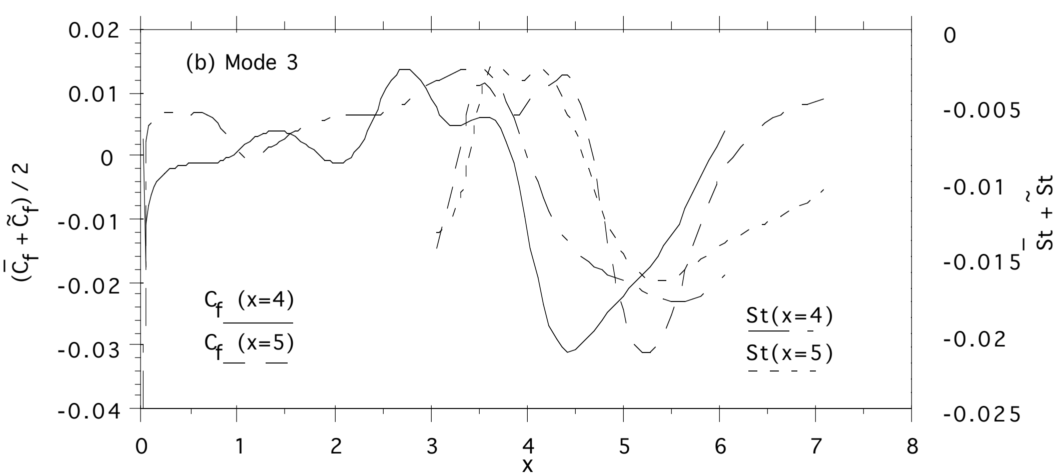

Figure 20: Comparison of the relative maxima of phase averaged in $(\bar{C}_f+\tilde{C}_f)/2$ and $\bar{St}+\tilde{St}$ at x=4 and x=5 for (a) Mode 2; (b) Mode 3.

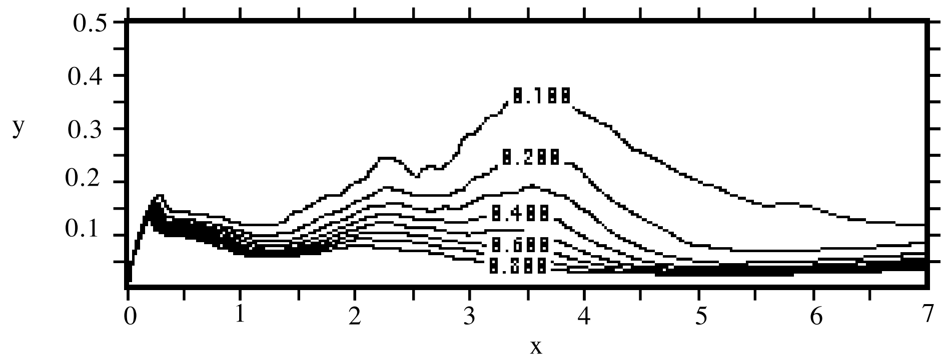

Figure 21: Contours of scalar fraction (defined as percentage of time $\phi < 0.5(\phi_\infty - \phi_w)$) in the separation and reattachment region.